Electronic Supplementary Material (ESI) for Analyst.

Supporting Information

Portable EIS based biosensor for the detection of microcystin-LR residues in environmental waterbodies and simulated bodyfluids

Atindra Kanti Mandal,[†,§] Tathagata Pal,[‡,§] Satish Kumar,[‡] Suparna Mukherji,[¶] and Soumyo Mukherji[*,‡]

†*Centre for Research in Nanotechnology and Science, Indian Institute of Technology Bombay, Mumbai, India*
‡*Department of Biosciences and Bioengineering, Indian Institute of Technology Bombay, Mumbai, India*
¶*Environmental Science and Engineering, Indian Institute of Technology Bombay, Mumbai, India*
§*These authors have contributed equally to this work*

*Corresponding Author (E-mail): mukherji@iitb.ac.in,soumyo.mukherji@gmail.com

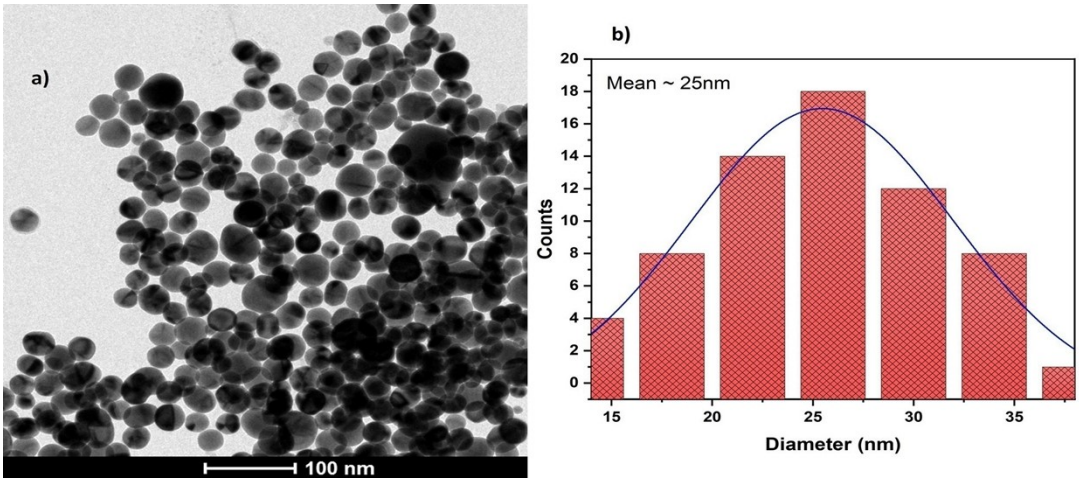

Figure S1: TEM image of cysteamine capped gold nanoparticles. a) TEM image. b) Histogram of particle size with a mean diameter of about 25nm.

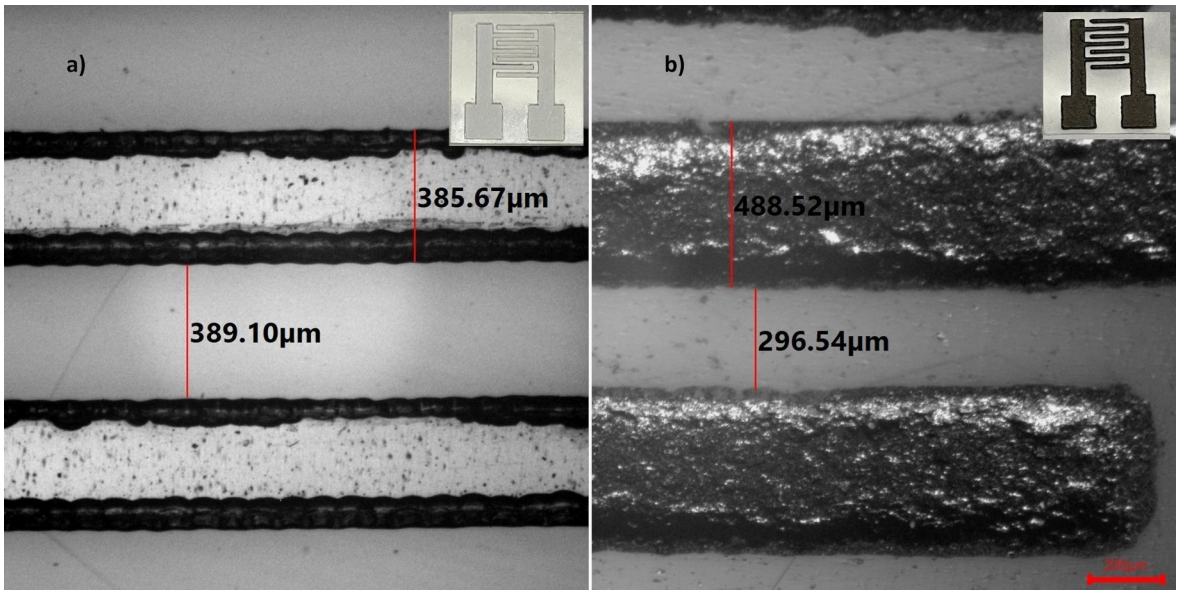

Figure S2: Stencil printed carbon interdigitated microelectrodes.a) Optical microscope image of stencil fabricated on a PET sheet. Inset: Image of stencil on PET sheet. b) Optical microscope image of Carbon electrodes on a PET sheet. Inset: Image of carbon electrodes on PET sheet.

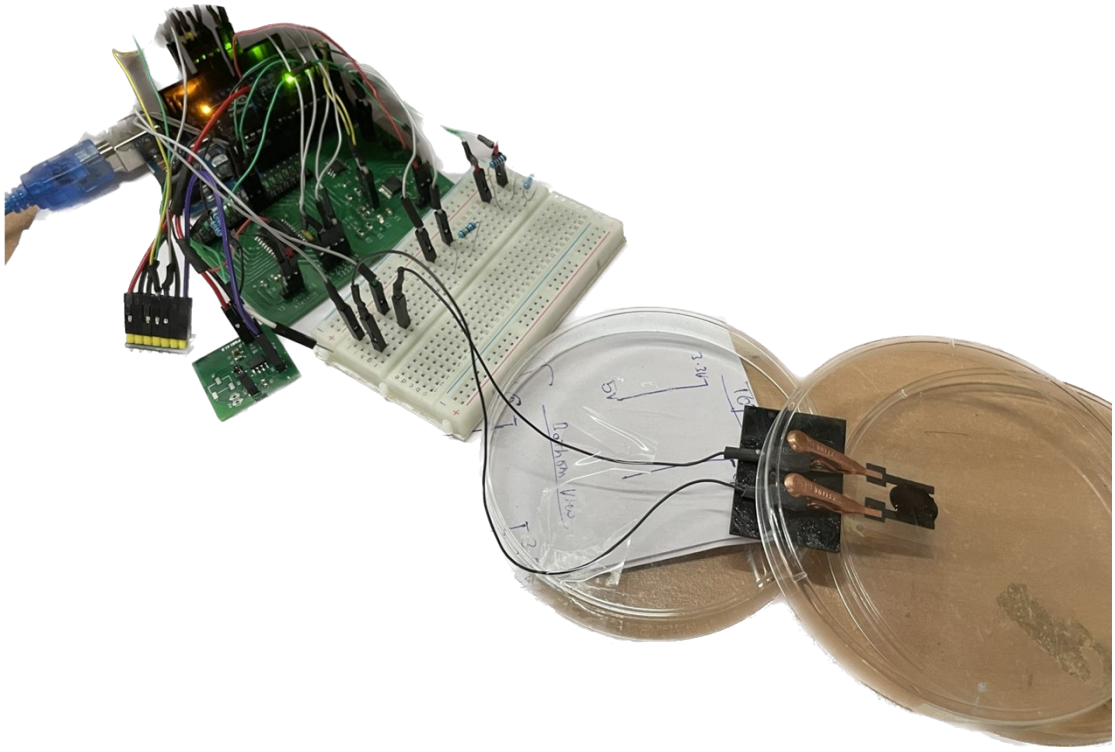

Figure S3: Internal Circuitry of the Device optimised at 100Hz

Figure S4: MCLR were spiked in water samples from Vihar lake in Mumbai and Ganges river in Kanpur, India and sensors were tested thereafter.

Figure S5: Image captured around Vihar Lake to evaluate the robustness and field deployability of ImAnalyzer.

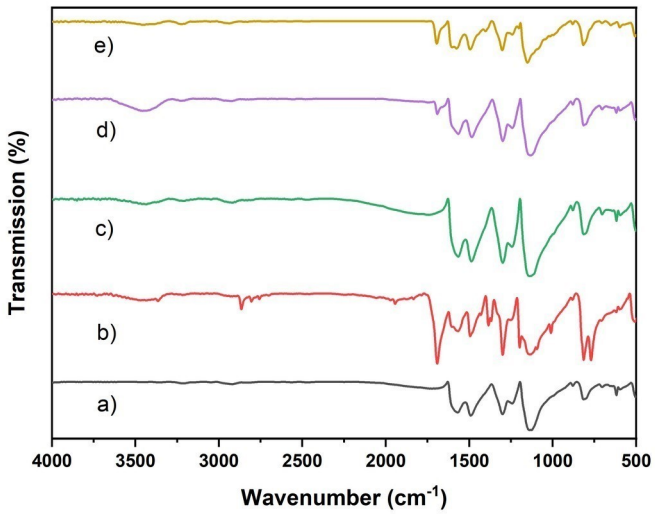

Figure S6: FTIR spectra of a) Polyaniline washed in DI, b) Polyaniline linked with terephthaldehyde, c) Composite of polyaniline and cysteamine capped GNP, d) Composite of polyaniline and cysteamine capped GNP linked with terephthaldehyde, e) Antibody immobilised on a terephthaldehyde treated Composite of polyaniline and cysteamine capped GNP

To investigate the changes in the molecular structure of the PAni backbone following treatment with terephthaldehyde and antibodies, FTIR spectroscopy was used in the current investigation. At different stages mid-IR spectra of PAni nanofibers, including DI water washed PAni, terephthaldehyde treated composite of PAni and cyateamine capped gold nanoparticles, and antibody immobilized PAni were obtained. The spectra were collected at each stage using a Bruker (Germany) 3000 Hyperion Microscope with Vertex 80 FTIR System with a scan rate of 32 and a resolution of 4 cm^{-1}.

In Fig. S6(a), 810 cm^{-1} represents out of plane -C-N stretching of 1,4 Para disubstituted benzene ring and out-of-plane bending of C-H bond in the aromatic ring. At 1578 cm^{-1} C=N stretching of the quinoid ring, at 1492 cm^{-1} stretching of the benzenoid ring happens. At 1295 cm^{-1} C-N stretching of the benzenoid ring is observed and at 1147 cm^{-1} in-plane C-H bending motion of the quinoid ring is observed (Subramanian et al., 2014). 1145 cm^{-1} denotes B-N+H-B stretching vibrations as well as doping and protonation of imine Nitrogen C=N (Chabukswar et al., 2001). 1307 cm^{-1} represents aromatic C-N stretching vibrations. In Fig. S6 (b) the stretching frequency at 1690 cm^{-1} indicate the formation of the imine link in the polymer (Larkin, Chapter 7, Elsevier, 2018). Thus, in Fig. S6 (b,d,e) -NH band II of the polymer is observed at around 1690 cm^{-1} (A. Murugesen et al., 2012). In Fig. S6(e), it keeps all of the amine and aldehyde interaction peaks since the antibody's amine end binds to terephthaldehyde's aldehyde group. After antibody attachment, a peak shift from 619 cm^{-1} to 596 cm^{-1} can be attributed to changes in the polymer's backbone caused by ions being intercalated into the polymer matrix (Pal et al., 2023).

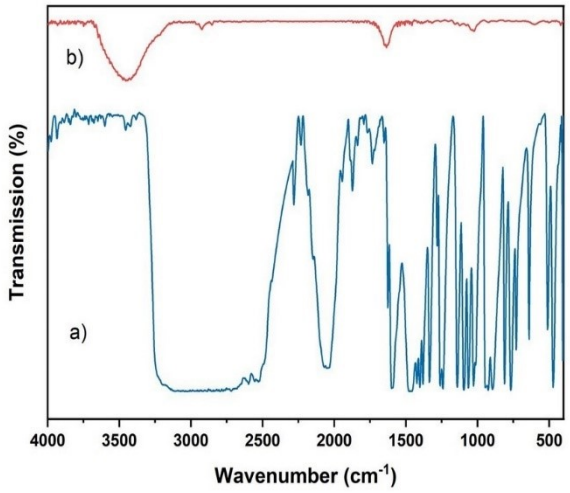

Figure S7: FTIR spectra of a) Cysteamine powder. b) Cysteamine capped gold nanoparticle

In Fig. S7(b) the presence of OH- groups of hydroxides from the surface of the nanoparticle is indicated by a broad band at about 3400 cm^{-1}. The bend in the amine group of cysteamine is indicated by a tiny peak at about 1072 cm^{-1}. Peaks at 1259 cm^{-1} are caused by C=N and C-N, whereas peak at 1634 cm^{-1} is due to gold (Shukri et al., 2016). In Fig. S7(a) confirmation of the presence of the -SH group in the cysteamine molecule is provided by a faint band about 2550 cm^{-1}. Notably, the band caused by -SH was not seen in the spectra of gold nanoparticles with cysteamine capping, confirming the S-Au interaction. (Aryal et al., 2006).

Table ST1: Comparison table for different techniques to detect Microcystin-LR

Method	Technique	Limit of Detection (ug/L)	Linear Range (ug/L)	Fabrication Method	Portability	Cost	Ref
HPLC		0.00075			Not portable	Very Expensive	7
LC/MS/MS		0.003			Not portable	Very Expensive	8
AuNCs/MoS2/ Ab/MCLR	DPV	0.0003	0.001–1000	(MoS2) nanosheets/ BSA-stabilized gold nanoclusters (AuNCs) composite and Au core/Pt shell nanoparticles (Au@PtNPs) on gold electrodes	Not mentioned	Expensive	9
SiO2@G-quadruplex	PEC	0.0007	0.001–1000	CdS/B-TiO2 nanorods as photoelectrode and electrodeposition of AuNP on GCE as bioelectrode	Not mentioned	Expensive	10

CDNA-MNPs	SERS	0.002	0.01 to 200	AuNPs modified MC-LR aptamer and Raman reporter as SERS probes while MNPs with cDNA of MC-LR aptamer as capture probes.	Not mentioned	Expensive	11
Aptamer-based microcantilever	Deflection measurement	1	Jan-50	Aptamer immobilised over microcantilever array (Micromotive GmbH, Mainz, Germany)	Not mentioned	Expensive	12
Graphene,multi-enzyme functionalised CNS	CV	0.016	0.05-15	Graphene sheet on enzyme functionalised carbon nano sphere (CNS)	Not mentioned	Moderate	13

MWCNT on GCE	CV	0.0017	0.005-1.0	Composite of room temperature ionic liquid (RTIL) and MWCNT on GCE	Not mentioned	Moderate	14
AuNP embedded Pani on stencil printed carbon IDEs	EIS	0.1	0.1-100	AuNP and Pani composite over stencil printed IDEs with conductive carbon ink	Portable and field deployable	Very Cheap	This work

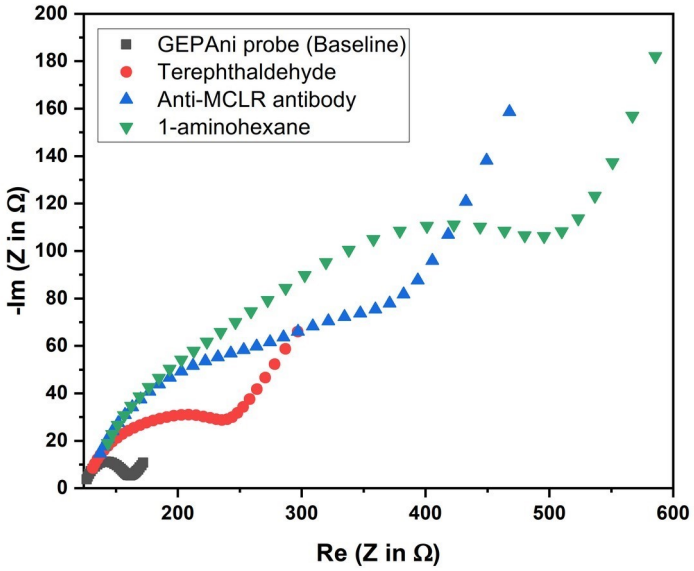

Figure S8: Nyquist plot for characterisation of substrate during functionalisation steps

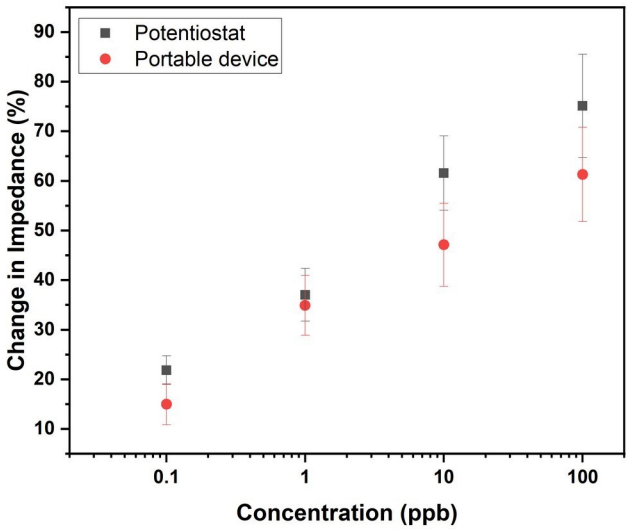

Figure S9: Relative change in impedance from baseline for MCLR constituted in PBS for Autolab (potentiostat) and custom portable device.

On comparison of potentiostat (having a FRA32M frequency analyser module from autolab) data with the portable device (Fig. S9) it was observed that the portable device has a lower response. This deviation compared to the potentiostat increases with increasing concentration of the analyte. It occurs due to the low frequency limitation of the device. At lower frequencies the portable device cannot accurately evaluate the impedance values due to the spectral leakage in the frequency analyser circuit. That is why for experiments on the portable device, the frequency was restricted to 100Hz and maximum concentration of the analyte to 100ppb to keep the deviation to the minimum.

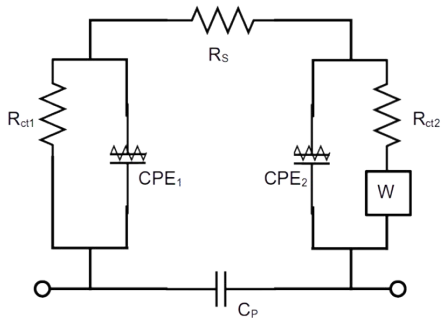

Figure S10: A modified Randles' equivalent circuit obtained using Nova software for the proposed sensor to detect MCLR. Rs denotes the solution resistance. Rct1 and CPE1 denotes the charge transfer resistance and constant phase element for one electrode whereas Rct2 and CPE2 for the other. W is added to include diffusion effect. Cp is due to parasitic or geometric reasons.

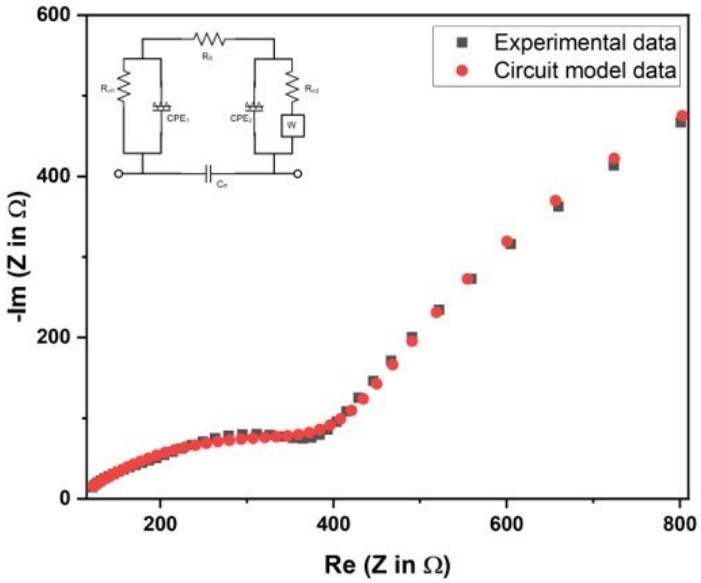

Figure S11: Nyquist plot of experimental data and the simulated values from equivalent circuit model. **Inset:** equivalent circuit.

Table ST2: Electrochemical parameters of the sensor for multiple concentrations of analyte (MCLR)

Concentration	CPE1 (umho)	n1	Rct1 (ohms)	Rs (ohms)	CPE2 (umho)	n2	Rct2 (ohms)	W (umho)	Cp (pF)
1ppb	27.1	0.57	193.4	114.8	277.2	0.73	1.21k	1171	0.9
10ppb	31.9	0.57	329.7	117.4	191.6	0.80	3.01k	962.4	193.2
100ppb	35.1	0.58	479.8	115.8	140.3	0.85	4.76k	587.3	95.6
1000ppb	36.2	0.6	619	121.4	58.8	0.92	6.99k	330	285

The sensor response is mainly based on the change in capacitance and charge transfer resistance due to the binding of the analyte with the electrodes. This change is captured in terms of impedance. Although, other parameters such as solution resistance, double layer capacitance and diffusion limited effects may also impact the overall impedance. Multiple literatures [15]-[18] were reviewed to design an initial circuit for running simulations in the Nova software from Metrohm. After, multiple iteration in the circuit model, best fit was obtained by the model shown in Fig. S10. In this circuit, Rct1 and CPE1 denote the charge transfer resistance and double layer capacitance at one electrode. Constant phase element (CPE) was used instead of pure capacitive element because of the roughness of the electrodes and non ideal behaviour. Together these represented analyte binding at one electrode [15],[19]. Similar elements were also selected for the other electrode to represent analyte binding but an additional warburg impedance (W) was included to incorporate any diffusion limited effects. Finally, capacitance Cp was included to incorporate any parasitic or geometric effects [18].

From the simulated results the fit was found to be adequate (Fig. S11). From Table. ST2 it can be observed that the overall impedance was dependent on multiple parameters. There was not much change in solution resistance (Rs) denoting it did not have much of an impact on the overall increase in impedance. This might be because all the measurements were performed in 10 mM $K_3(Fe(CN)_6/K_4Fe(CN)_6$ solution. The charge transfer

resistance for both the electrodes (Rct1, Rct2) increased with an increase in the concentration of the analyte indicating analyte binding. The constant phase element (CPEs) also had an effect on the overall impedance as it also varies with increasing concentration of the analyte. This signifies that analyte binding might also have a capacitive effect. Diffusion effect (W) do play role but generally their major impact is felt from 10Hz and below [20],[21].

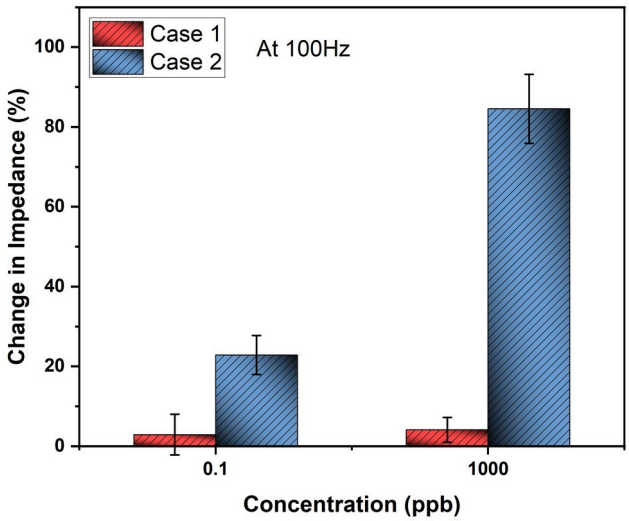

Figure S12: Experiment showcasing blocking performance of hexylamine. **Case1:** GEPAni probe with terephthaldehyde then blocked with 1-aminohexane (hexylamine). **Case2:** GEPAni probe with terephthaldehyde immobilised with antiMCLR antibody and then blocked with 1-aminohexane (hexylamine).

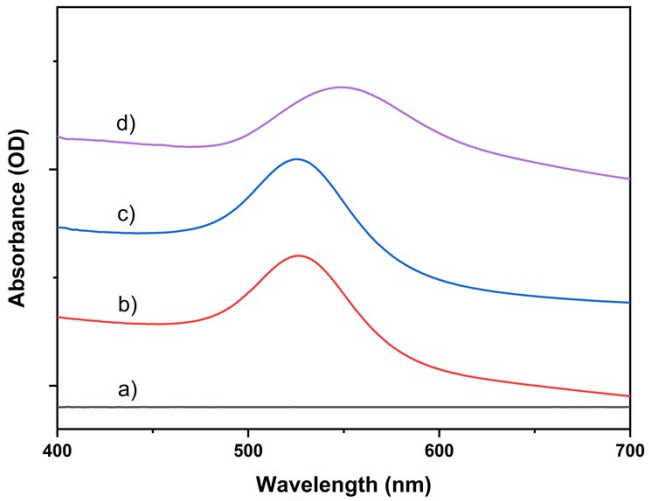

Figure S13: UV-Visible spectra of: a) DI water. b) Cysteamine capped gold nanoparticles. c) Cysteamine capped gold nanoparticles linked with terephthaldehyde. d) Antibodies immobilised over cysteamine capped gold nanoparticles linked with terephthaldehyde.

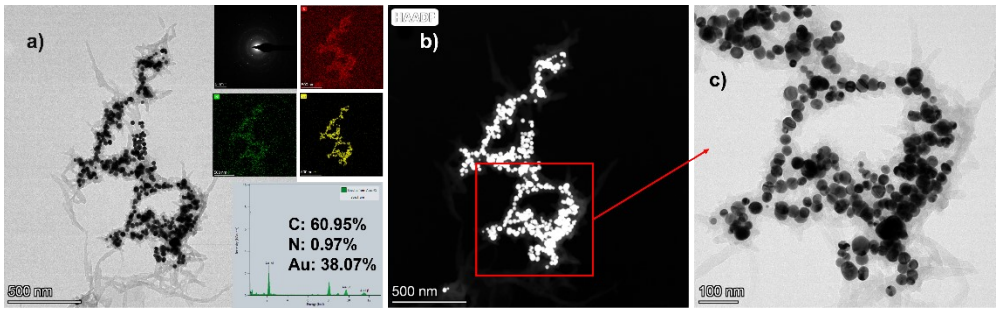

Figure S14: Electron microscope image of cysteamine capped gold nanoparticles embedded in polyaniline. **a)** FEGTEM image of cysteamine capped gold nanoparticles embedded in polyaniline. **a Inset:)** Diffraction pattern showing the crystalline nature and EDAX showing the different percentages of the material. **b)** Dark field TEM image showing the location of cysteamine capped gold nanoparticles intercalated in polyaniline. **c)** Higher magnification image showing the morphology of cysteamine capped gold nanoparticles embedded in polyaniline.

Supplementary Material References

[1] S. Subramanian, S. Narayanasastri, and A. R. K. Reddy, “Doping-induced detection and determination of propellant grade hydrazines by a kinetic spectrophotometric method based on nano and conventional polyaniline using halide ion releasing additives,” RSC Adv., vol. 4, no. 52, pp. 27404–27413, Jun. 2014, doi: 10.1039/C4RA02296C.

[2] Chabukswar V V., Pethkar S, Athawale AA. Acrylic acid doped polyaniline as an ammonia sensor. Sensors Actuators B Chem 2001;77:657–63. https://doi.org/10.1016/S0925-4005(01)00780-8

[3] A. Murugesan, T. Vidhyadevi, S. S. Kalaivani, M. P. Premkumar, L. Ravikumar, and S. Sivanesan, “Kinetic and thermodynamic studies on the removal of Zn2+ and Ni2+ from their aqueous solution using poly(phenylthiourea)imine,” Chemical Engineering Journal, vol. 197, pp. 368–378, Jul. 2012, doi: 10.1016/j.cej.2012.05.027.

[4] T. Pal, S. Aditya, T. Mathai, and S. Mukherji, “Polyaniline coated plastic optic fiber biosensor for detection of aflatoxin B1 in nut, cereals, beverages, and body fluids,” Sensors and Actuators B: Chemical, vol. 389, p. 133897, Aug. 2023, doi: 10.1016/j.snb.2023.133897.

[5] W. N. W. Shukri, N. Bidin, S. Islam, G. Krishnan, M. A. A. Bakar, and M. S. Affandi, “Synthesis and characterization of uncoated and cysteamine-coated gold nanoparticles by pulsed laser ablation,” JNP, vol. 10, no. 4, p. 046007, Oct. 2016, doi: 10.1117/1.JNP.10.046007.

[6] S. Aryal, R. B.k.c., N. Dharmaraj, N. Bhattarai, C. H. Kim, and H. Y. Kim, “Spectroscopic identification of SAu interaction in cysteine capped gold nanoparticles,” Spectrochimica Acta Part A: Molecular and Biomolecular Spectroscopy, vol. 63, no. 1, pp. 160–163, Jan. 2006, doi: 10.1016/j.saa.2005.04.048.

[7] L. Lian, T. Guo, Y. Wu, L. Jin, D. Lou, D. Sun Chin.,”Determination of Microcystin-LR in Environmental Water by Magnetic Solid Phase Extraction-High Performance Liquid Chromatography”, J. Anal. Chem., 12 (2015), pp. 1876-1881, doi.org/10.1016/S1872-2040(15)60884-2

[8] H. Yu, K.D. Clark, J.L. Anderson J., “Rapid and sensitive analysis of microcystins using ionic liquid-based in situ dispersive liquid–liquid microextraction”, Chromatogr. A, 1406 (2015), pp. 10-18, doi.org/10.1016/j.chroma.2015.05.075

[9] P. Pang, X. Teng, M. Chen, Y. Zhang, H. Wang, C. Yang, W. Yang, C.J. Barrow, “Ultrasensitive enzymefree electrochemical immunosensor for microcystin-LR using molybdenum disulfide/gold nanoclusters
nanocomposites as platform and Au@Pt core-shell nanoparticles as signal enhancer”, Sens. Actuators B Chem., 266 (2018), pp. 400-407, 10.1016/j.snb.2018.03.154

[10] A. Qileng, Y. Cai, J. Wei, H. Lei, W. Liu, S. Zhang, Y. Liu, ”Construction of CdS/B-TiO2 nanorods photoelectrochemical immunosensor for the detection of microcystin-LR using SiO2@G-quadruplex as multiamplifier”, Sens. Actuators B Chem., 254 (2018), pp. 727-735, 10.1016/j.snb.2017.07.164

[11] Deyun He, Zhengzong Wu, Bo Cui, Zhengyu Jin, “A novel SERS-based aptasensor for ultrasensitive sensing of microcystin-LR”, Food Chemistry, Volume 278, 2019, Pages 197-202, doi.org/10.1016/j.foodchem.2018.11.071

[12] Guangping Zhang, Chao Li, Shangquan Wu, Qingchuan Zhang, “Label-free aptamer-based detection of microcystin-LR using a microcantilever array biosensor”, Sensors and Actuators B: Chemical, Volume 260, 2018, Pages 42-47, doi.org/10.1016/j.snb.2017.12.112

[13] H. Zhao, J. Tian and X. Quan, “A graphene and multienzyme functionalized carbon nanosphere-based electrochemical immunosensor for microcystin-LR detection”, Colloids and Surfaces B: Biointerfaces, 2013, 103, 38–44, dx.doi.org/10.1016/j.colsurfb.2012.10.010

[14] X. Sun, L. Guan, H. Shi, J. Ji, Y. Zhang and Z. Li, “Determination of microcystin-LR with a glassy carbon impedimetric immunoelectrode modified with an ionic liquid and multiwalled carbon nanotubes”, Microchimica Acta, 2013, 180, 75–83, dx.doi.10.1007/s00604-012-0912-4

[15] Z. Li, Z. Ye, Y. Fu, Y. Xiong and Y. Li, “A portable electrochemical immunosensor for rapid detection of trace aflatoxin B1 in rice”, Analytical Methods, 2016, 8, 548–553, 10.1039/c5ay02643a

[16] F. Lisdat and D. Schäfer, “The use of electrochemical impedance spectroscopy for biosensing”, Analytical and Bioanalytical Chemistry, 2008, 391, 1555–1567

[17] Z. He and F. Mansfeld, “Exploring the use of electrochemical impedance spectroscopy (EIS) in microbial fuel cell studies”, Energy & Environmental Science, 2009, 2, 215–219

[18] L. C. T. Shoute et al., “Label-free impedimetric immunosensor for point-of-care detection of COVID-19 antibodies,” Microsyst Nanoeng, vol. 9, no. 1, Art. no. 1, Jan. 2023, doi: 10.1038/s41378-022-00460-5.

[19] H.-W. Jung, Y. W. Chang, G. Lee, S. Cho, M.-J. Kang, and J.-C. Pyun, “A capacitive biosensor based on an interdigitated electrode with nanoislands,” Analytica Chimica Acta, vol. 844, pp. 27–34, Sep. 2014, doi: 10.1016/j.aca.2014.07.006

[20] T. Q. Nguyen and C. Breitkopf, “Determination of Diffusion Coefficients Using Impedance Spectroscopy Data,” J. Electrochem. Soc., vol. 165, no. 14, p. E826, Nov. 2018, doi: 10.1149/2.1151814jes

[21] S.-B. Yoon, J.-P. Jegal, K. C. Roh, and K.-B. Kim, “Electrochemical Impedance Spectroscopic Investigation of Sodium Ion Diffusion in MnO2 Using a Constant Phase Element Active in Desired Frequency Ranges,” J. Electrochem. Soc., vol. 161, no. 4, p. H207, Feb. 2014, doi: 10.1149/2.046404jes.

[22] P. J. Larkin, “Chapter 7 - General Outline for IR and Raman Spectral Interpretation,” in Infrared and Raman Spectroscopy (Second Edition), P. J. Larkin, Ed., Elsevier, 2018, pp. 135–151. doi: 10.1016/B978-0-12-804162-8.00007-0

[23] T. A. Munyayi, B. C. Vorster, and D. W. Mulder, “The Effect of Capping Agents on Gold Nanostar Stability, Functionalization, and Colorimetric Biosensing Capability,” Nanomaterials, vol. 12, no. 14, Art. no. 14, Jan. 2022, doi: 10.3390/nano12142470.